

<sup>1</sup> Ocean Mesoscale Mixing linked to Climate Variability

<sup>2</sup> **One-sentence summary:**

<sup>3</sup> Mesoscale mixing in the ocean is connected to the large scale climate, due to mixing  
<sup>4</sup> suppression by the large scale flow.

<sup>5</sup> Julius Busecke<sup>1\*</sup>, Ryan P. Abernathey<sup>2</sup>

<sup>1</sup>Princeton University, Princeton, New Jersey, USA

<sup>2</sup>Lamont-Doherty Earth Observatory of Columbia University, Palisades, New York, USA

\*Corresponding author; E-mail: jbusecke@princeton.edu.

<sup>6</sup> **Mesoscale turbulence in the ocean strongly impacts the circulation, water mass**  
<sup>7</sup> **formation, and the transport of tracers. Little is known, however, about how**  
<sup>8</sup> **mixing varies on climate timescales.**

<sup>9</sup> **We present the first time-resolved global dataset of lateral mesoscale eddy dif-**  
<sup>10</sup> **fusivities, obtained by applying Suppressed Mixing Length Theory to satellite-**  
<sup>11</sup> **observed geostrophic velocities. The diffusivities exhibit interannual variabil-**  
<sup>12</sup> **ity throughout the global ocean, regionally correlated with climate indices like**  
<sup>13</sup> **ENSO, NAO, DMI and PDO. The effects of variable mixing length, driven by**  
<sup>14</sup> **variations in the large scale flow, often exceed the effect of variations in local**  
<sup>15</sup> **eddy kinetic energy, previously thought of as the main driver of variability in**  
<sup>16</sup> **eddy mixing.**

<sup>17</sup> **This mode of variability of surface mixing, not currently represented in global**

18       **climate models, could have far reaching consequences for the oceanic distribu-**  
19       **tion of heat, salt and carbon in the global ocean, regional dynamics like ENSO**  
20       **variance and ecosystem dynamics.**

## 21     1 Introduction

22     Mesoscale turbulence (on scales from 50-200 km) is ubiquitous in the ocean and strongly im-  
23     pacts the meridional overturning circulation (1, 2), water mass formation (3), and the transport  
24     of tracers like heat, salt, nutrients, oxygen and anthropogenic carbon (4–7), as well as regional  
25     dynamics like ENSO variance (8) and ecosystem dynamics.

26     Diffusion coefficients quantify the rate at which mixing processes transport tracers and are  
27     used in coarse-resolution climate models to represent unresolved transport processes. Past work  
28     on mesoscale mixing has focused on estimating the long-term mean diffusivity and its spatial  
29     variability (9–12). The flanks of western boundary currents exhibit diffusivities up to 10000  
30     m<sup>2</sup> s<sup>-1</sup> while values on the order of 100 m<sup>2</sup> s<sup>-1</sup> are found in the subtropical gyres. Employing  
31     such spatially variable diffusivities, rather than constant values, in global climate models (7) or  
32     inverse methods (13) strongly affects the estimated ocean uptake of carbon and rates of water  
33     mass formation. It is thus critical to investigate if and how mesoscale diffusivities change over  
34     time, a possibly missing element in future climate projections.

35     Persistent periods of increased/decreased mesoscale mixing could have a major impact on  
36     the transport of ocean tracers, particularly when these periods are connected to other fluctuating  
37     components of the climate system. This applies to both interannual to decadal climate vari-  
38     ability as well as forced trends due to anthropogenic release of carbon dioxide. However, there  
39     have been very few studies of the interannual variability in the mesoscale mixing process (14).  
40     A recent study of the global sea surface salinity maxima found evidence for large scale changes  
41     of surface diffusivities in the subtropical gyre of the South Pacific (15), but the methods used

42 in that study are not suited to produce global maps of Eulerian diffusivity. In this study we  
43 apply suppressed mixing length theory (SMLT) to large-scale velocities derived from satellite  
44 altimetry to produce temporally variable global maps of surface diffusivities.

45 In earlier work (9), the Osborn-Cox diffusivity was applied to diagnose the mixing of numer-  
46 ically simulated passive tracers by the surface-geostrophic flow observed by satellite altimetry.  
47 These kinematic experiments provided an estimate of the time-mean diffusivity over the entire  
48 satellite record. Our initial approach to estimating temporal variability was to use the Osborn-  
49 Cox diffusivity directly in a time-dependent way. However, we discovered that a subtle and  
50 unavoidable artifact of the data processing necessary to produce velocities suitable for numer-  
51 ical tracer advection (removal of the divergence and adjustment to satisfy kinematic boundary  
52 conditions) introduced spurious basin-scale temporal variability in the flow (for details see Sup-  
53 plementary Materials). This spurious variability averages out for the long-term mean, but it  
54 does bias the temporal variability, such that we cannot rely on the tracer experiments to pro-  
55 vide a realistic estimate. Instead, we use these experiments as a test-bed to validate the SMLT  
56 closure for diffusivity, and then apply the SMLT to the true, un-biased observations to infer to  
57 correct temporal variability in diffusivity.

58 The core concept of mixing length theory (16) is that the eddy diffusivity ( $K$ ) is proportional  
59 to the product of an eddy-velocity  $u_{rms} = \sqrt{2EKE}$  (with the eddy kinetic energy  $EKE =$   
60  $\sqrt{u^2 + v^2}$ ), an O(1) constant mixing efficiency  $\Gamma$ , and a mixing length  $L$ , which in isotropic  
61 turbulence without mean flow is assumed to be the eddy length scale (e.g. eddy diameter)  
62  $L_{eddy}$ :

$$K = \Gamma L u_{rms} \quad (1)$$

63 SMLT was developed to account for the role of large-scale mean flow and eddy propagation  
64 in modulating mixing rates. In the presence of a mean flow and eddy propagation, the mixing

65 length is suppressed and is smaller than the eddy size  $L_{eddy}$ , such that

$$L = L_{eddy}S \quad (2)$$

66 where  $S \leq 1$  is a suppression factor (17, 18). In the original theory of Ferrari and Nikurashin  
67 (2010), which applies to axisymmetric zonal jets (17)

$$S = \frac{1}{1 + \alpha(c - U)^2} \quad (3)$$

68 where  $U$  is the zonal mean flow,  $c$  is the zonal eddy phase speed, and  $\alpha = k^2/\gamma^2$ , with zonal  
69 wavenumber  $k = 2\pi/L_{eddy}$  and decorrelation timescale  $\gamma$ . Subsequent work suggested writing  
70 the diffusivity as

$$K = K_0 S \quad (4)$$

71 where  $K_0 = \Gamma L_{eddy} u_{rms}$  is the *unsuppressed diffusivity* (18). An important conclusion from  
72 this formula is that both the small-scale (mesoscale) turbulent flow (represented by  $K_0$ ) and the  
73 large-scale background flow (related to  $S$ ) conspire to determine the diffusivity.

74 This framework has been employed to explain the spatial variability of mesoscale mixing  
75 rates within the Antarctic Circumpolar Current (17), a broad sector of the Eastern Pacific, and  
76 for the global ocean (18). These results agree well with studies using idealized tracer experi-  
77 ments (9) and Argo float data (12), all showing large spatial variability of eddy mixing in the  
78 ocean.

79 This body of research suggests that even small amplitude variability in the large scale flow  
80 can have a major impact on the diffusive transport of tracers near the surface. Furthermore, sev-  
81 eral studies indicate that isopycnal diffusivity throughout the pycnocline is closely correlated  
82 with near surface mixing rates (12, 19). Together, this implies that small changes in the large

83 scale flow, due to natural variability or a changing climate, could have strong effects on pro-  
84 cesses which are sensitive to isopycnal tracer transport by mesoscale mixing, both at the surface  
85 and at depth.

86 All of the above results hold for long term mean estimates, but how big is the influence of  
87 variable surface flow on mixing rates? Can SMLT be used to diagnose interannual variability in  
88 mixing rates?

89 To investigate these questions, we first compared the estimate of SMLT to a direct calcula-  
90 tion of cross frontal mixing, using the Osborn-Cox diffusivity, in an idealized tracer experiment  
91 with interannual variability. The Osborn-Cox diffusivity is derived from the high-resolution  
92 numerical advection of simulated tracers and is thus independent from the SMLT estimate. The  
93 appeal of the SMLT is that it does not require high resolution tracer fields, but instead is based  
94 on the the large scale flow and mesoscale velocity statistics, without the need for any correc-  
95 tions to the velocity field. These velocity observations exist since the early 1990's and enable  
96 us to estimate surface diffusivities from a simple formula based on observational data for a time  
97 period of over 20 years. SMLT also offers a mechanistic interpretation for variations in diffusiv-  
98 ity which may form the basis for future parametrizations of lateral mixing in coarse-resolution  
99 ocean models.

100 The results (described in detail in the Methods section) indicate that both methods agree very  
101 well when describing relative temporal changes in surface mixing. Discrepancies exist mostly  
102 in the form of constant offsets and different amplitude of temporal changes, with estimates  
103 from the Osborn-Cox method usually being larger with a stronger amplitude. This mirrors the  
104 findings of previous work (9, 12, 18), which show strong agreement in spatial patterns of mixing  
105 rates, while the absolute values are much less constrained. The strong correlation between our  
106 two independent estimates however, indicates that the SMLT is able to capture the underlying  
107 characteristics of interannual variability in mesoscale mixing.

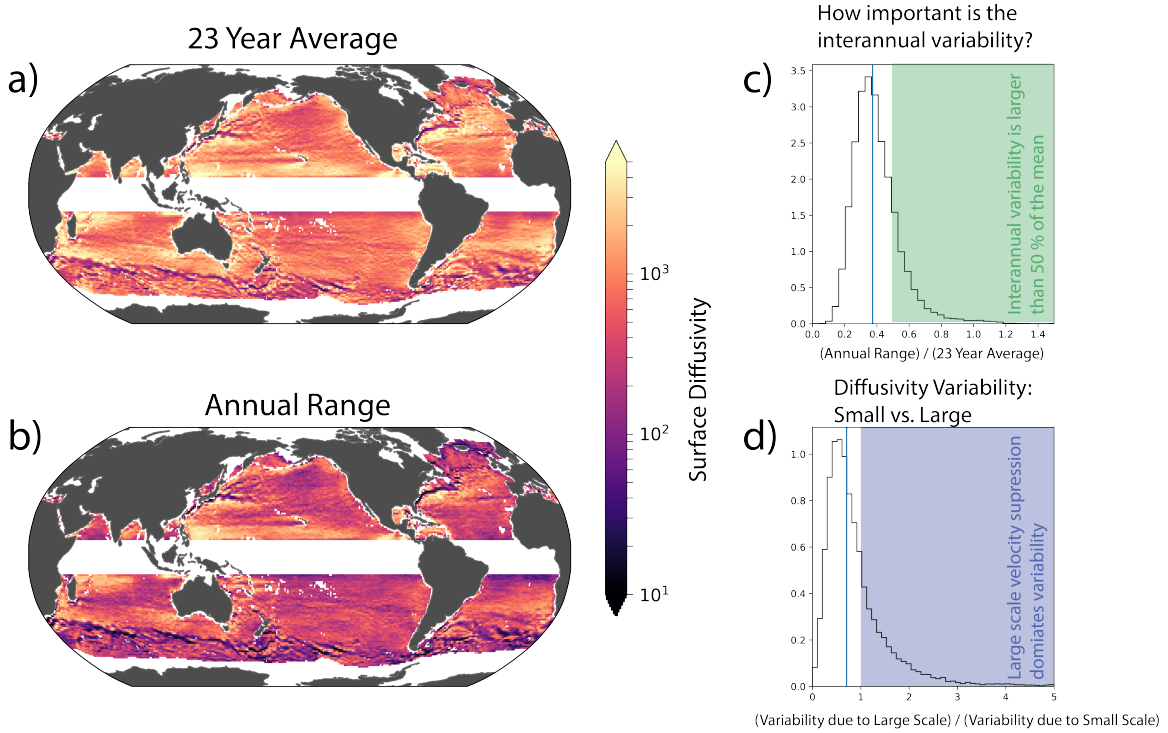


Figure 1:  $K_{mix}$  mean and annual range. The maps (a-b) show surface diffusivity [ $m^2/s$ ] from suppressed mixing length theory applied to observed surface velocities. a) Full record (23 years) average. b) Annual range, defined as the difference between the 90th and 10th percentile of annual averages. c) Histogram of the ratio of b) over a), indicating that in many parts of the ocean interannual variability is a sizeable fraction of the mean. d) Same as c) but for the ratio of standard deviations due to the large scale velocity suppression over small scale (EKE) contribution to the variability of surface diffusivity. The vertical lines in c) and d) show the median of the distribution.

## 2 Results and Discussion

The surface diffusivity from SMLT ( $K_{mix}$ ), derived from Aviso velocities, is shown in Figure 1. The long term mean (Figure 1a) shows the familiar pattern of high diffusivities near the western boundary currents and low diffusivities within the subtropical gyres and the Antarctic Circumpolar current. The annual range (defined by the difference between the 10th and 90th percentile of the annual means, Figure 1b) shows a similar pattern. These results indicate that interannual

variability in surface diffusivities is large, on the order of 100-1000  $m^2/s$ . This represents a large fraction of the mean value in most of the global ocean. The ratio of interannual range to mean diffusivity is larger than 25% in most of the global ocean and in some regions over 50% (Figure 1c). The amplitude of variability suggests that capturing the temporal variability may be important for characterizing the effects of the mesoscale mixing process on the global ocean circulation. We now examine the mechanisms behind this variability and its relationship with large-scale climate.

SMLT suggests that very small amplitude variations in large scale velocities, caused by e.g. changes in the wind forcing, result in relatively large changes of diffusivity. It is hence very plausible that large-scale climate fluctuations (20) and anthropogenic changes (21) lead to changes in both large scale circulation as well as eddy activity, both of which affect surface diffusivities. Indeed, we find that in many regions of the world ocean, there is a strong relation between large scale climate indices and the surface diffusivity, as shown in Figure 2.

In the Western Equatorial Pacific,  $K_{mix}$  values are significantly elevated during positive NINO3.4 periods. Increases up to  $800m^2/s$  are diagnosed in the Southwest subtropical Pacific; these increases are due almost entirely to variations in  $S$  caused by the large scale flow. A recent climate modeling study concluded that larger lateral diffusivity leads to larger ENSO variance in the tropical Pacific (8). They showed that enhanced lateral diffusivity leads to stronger vertical and weaker lateral temperature gradients, both enhancing the coupling between ocean and atmosphere. Our results suggest that lateral diffusivity is positively correlated with ENSO events, particularly in parts of the subtropical Pacific (Figure 2), with amplitudes of changes on similar or larger than the range of constant diffusivity values used in that study. We speculate that such interannual variations in lateral mixing may therefore play a role in modulating ENSO dynamics, particularly since the variability has a non uniform (western intensified) pattern, which in the South Pacific even shows a change in correlation towards the East, how-

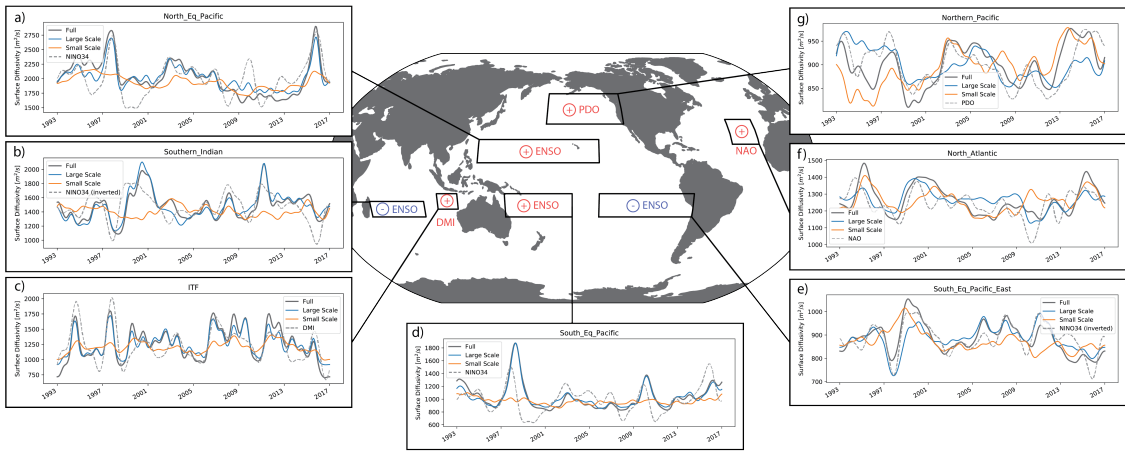


Figure 2: Relation of  $K_{mix}$  to large scale climate variability. Map shows simplified schematic of the relationship of several climate indices to the surface diffusivities. Red/blue indicates a positive/negative correlation with the respective index. All panels show timeseries of  $K_{mix}$  (black), the contribution of large scale velocity to  $K_{mix}$  (blue), the contribution of small scale velocities to  $K_{mix}$  (orange) and a selected climate index (gray), indicated in the legend and within the map box. The climate index is normalized with the mean and standard deviation of the  $K_{mix}$  timeseries for visual comparison, thus no units are given. Boxes used for averaging of each time series are indicated in map inset. All data shown are smoothed with a 4 month Gaussian window.

<sup>139</sup> ever with smaller amplitude (Fig 2e). Full investigation of the nature of this interaction would  
<sup>140</sup> require the introduction of time-dependent SMLT in an eddy parametrization and a coupled  
<sup>141</sup> climate model.

<sup>142</sup> Temporally variable lateral diffusivities might matter for other regions as well. In the south-  
<sup>143</sup> ern Indian Ocean surface diffusivities are suppressed during increased NINO3.4 episodes (Fig-  
<sup>144</sup> ure 2 ). In this region as well, changes in large-scale velocity characteristics account for the  
<sup>145</sup> majority of the observed variability, particularly with respect to the ENSO signal.

<sup>146</sup> Surface diffusivities do not just respond to ENSO, but also a variety of other climate indicies,  
<sup>147</sup> like the North Atlantic Oscillation (22) which correlates with diffusivities in the North Eastern  
<sup>148</sup> Subtropical gyre in the Atlantic (Figure 2f).

<sup>149</sup> In the outflow region of the Indonesian Througflow (ITF), we observe strong correlation  
<sup>150</sup> between the surface diffusivities and the DMI (Dipole Mode Index; (23)), seen in Figure 2c.  
<sup>151</sup> The region is critical for exchange of water from the Pacific to the Indian Ocean. It has been  
<sup>152</sup> shown that seasonal and large-scale climate fluctuations on the Pacific side and in the Indonesian  
<sup>153</sup> seas modulate the characteristics of the outflow water (24,25). Lateral diffusion at shallow depth  
<sup>154</sup> is essential for explaining the spreading of heat anomalies exiting the ITF into the Indian Ocean  
<sup>155</sup> (26,27). Variations in how the water from the ITF is distributed into the Indian Ocean can have  
<sup>156</sup> implications for ocean atmosphere interaction, including the Madden-Julian Oscillation (28).

<sup>157</sup> In the North Pacific, surface diffusivities show a relation to the Pacific Decadal Oscilation  
<sup>158</sup> (PDO, (29). The large scale component of the diffusivities shows a closer relation to the PDO  
<sup>159</sup> than the small-scale (EKE-based) contribution (Figure 2g). The resulting observed diffusivity  
<sup>160</sup> in this case is not dominated by the large scale contribution; instead it seems essential to capture  
<sup>161</sup> both components to represent the full time series.

<sup>162</sup> The examples above illustrates a key point of this study: the effects of variable large scale  
<sup>163</sup> flow are crucial in reproducing realistic changes in surface diffusivity. Suppression by the large

<sup>164</sup> scale flow is not the sole mechanism for variability—the EKE still plays a major role, as should  
<sup>165</sup> be expected—but regionally the effect of mixing suppression by the large scale flow can have a  
<sup>166</sup> comparable or even larger effect on mixing variability as effects of EKE, which is related to local  
<sup>167</sup> stratification via baroclinic instability (30). The latter is the only effect currently represented in  
<sup>168</sup> parameterizations for eddy transport in coarse resolution ocean models.

<sup>169</sup> Investigating in detail the regional effects of variable surface diffusivities will be the subject  
<sup>170</sup> of future manuscripts; instead here we aim to illustrate how variable mixing processes could be  
<sup>171</sup> crucial for a wide range of coupled climate phenomena.

### <sup>172</sup> 3 Conclusions

<sup>173</sup> In this study we present a novel dataset of surface diffusivities based on long-term global velocity  
<sup>174</sup> observations. We find strong evidence that mixing rates in the ocean vary on interannual  
<sup>175</sup> and longer time scales in many regions of the global ocean. The observed mixing rates suggest  
<sup>176</sup> a coupling between large scale climate variability and eddy mixing rates due to small amplitude  
<sup>177</sup> changes in the large scale flow. To our knowledge, such large-scale, coherent temporal variability  
<sup>178</sup> between mesoscale mixing and global climates modes has not been documented before.

<sup>179</sup> The vertical coherence of eddy velocities and transports over the upper 1000 m (31) implies  
<sup>180</sup> that the near-surface lateral mixing variability described here corresponds with isopycnal mixing  
<sup>181</sup> variability in the main thermocline (9). Due to the importance of lateral mesoscale mixing  
<sup>182</sup> for the ocean uptake of heat and carbon (7, 32, 33), the distribution of oxygen and nutrients in  
<sup>183</sup> the ocean (34, 35), ENSO dynamics (8) and water mass formation (3) we suggest that temporal  
<sup>184</sup> variability in mesoscale mixing could be an important climate feedback mechanism.

<sup>185</sup> This mechanism is not represented in eddy parametrizations for global climate and earth  
<sup>186</sup> system models, potentially biasing internal variability as well as long term trends in circulation,  
<sup>187</sup> water mass transformations, heat and tracer transport, ocean-atmosphere interaction and global

188 climate variability.

189 This becomes particularly important when looking at past and present climate states, where  
190 changes in circulation on the order of  $1\text{cm/s}$  seems very plausible in many parts of the ocean.  
191 The long term diffusivity trend over the observed period (1993-2017) supports this point: The  
192 trend in  $K_{mix}$  seems to be a superposition of different trend patterns for the large scale and  
193 small scale contributions to  $K_{mix}$  (Fig. 3). Using only one component of the velocity field  
194 would lead to a quite different long term evolution of the surface diffusivities. And while these  
195 linear trends might not represent a purely anthropogenic (e.g. forced) signal, they illustrate the  
196 need to account for the full interaction of large scale and small scale velocities to capture the  
197 effects of mesoscale mixing in the ocean.

198 Further research is needed to quantify the effects of variable mixing rates in coupled climate  
199 models, which will require more knowledge about the vertical structure of mixing rates and the  
200 suppression by large scale flow. Even though previous results suggest that increased surface  
201 diffusivity extends below the surface in the long-term mean (12, 19), the observed velocity data  
202 at depth is currently not sufficient to evaluate the suppressed mixing length theory (SMLT)  
203 globally.

204 While the agreement in terms of relative change for different methods for estimating mix-  
205 ing rates is very good, large offsets and differences in amplitude remain and require further  
206 research and observational constraints. Our kinematic tracer experiments revealed that short  
207 scale variations (seasonal to monthly) in EKE do not influence the diffusivity estimates, indi-  
208 cating that on those timescales the fundamental assumption for a diffusive approach - the local  
209 balance between tracer variance creation and dissipation - might not be valid anymore. For the  
210 results presented here, on interannual time scales and longer, the assumption holds (details are  
211 discussed in the Supplementary Material) but future work is needed to investigate the limits of  
212 a diffusive approach to parameterize the effect of mesoscale eddies in coarse resolution general

Surface Diffusivity - 23 Year Linear Trend

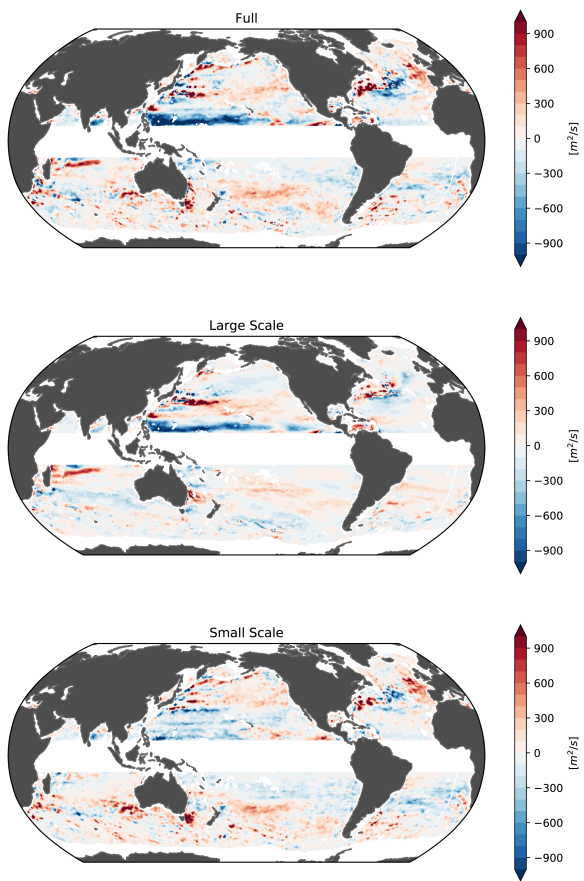


Figure 3: 23-year linear trend for  $K_{mix}$  and its components. — The total trend in diffusivity over the 23 year period is shown for the full  $K_{mix}$  (upper), the large-scale contribution (middle) and the small scale contribution (lower).

<sup>213</sup> circulation models.

214 **4 Data and Methods**

215 **4.1 Analysis Tools**

216 All analysis steps in this paper were performed with Python (<https://www.python.org>), in par-  
217 ticular the two packages xarray (36) and xgcm (37) were used extensively.

218 **4.2 Velocity data**

219 All velocity data in this study are estimates of geostrophic surface velocity based on altimetry  
220 (AVISO DUACS2014; produced by Ssalto/Duacs and distributed by Aviso, with support from  
221 Cnes, <http://www.aviso.altimetry.fr/duacs/>). The velocity record extends from January  
222 1993 until January 2017 (using the near real time product after May 2016).

223 **4.3 Velocity decomposition**

224 To investigate characteristics of the velocity field we need to decompose velocities into a small-  
225 scale (Mesoscale) and a large-scale component. We chose to use a combination of temporal and  
226 spatial filtering to reduce signals to 'true' mesoscale eddy signals.

227 This separation approach is applied for both methods described below, and if not otherwise  
228 stated overbars (primes) denote time averages (time deviations) which are additionally spatially  
229 lowpass (highpass) filtered with a Gaussian kernel equivalent to 200km.

230 **4.4 Tracer experiments**

231 The kinematic tracer experiments are conducted in an idealized 2D configuration of the MIT-  
232 gcm (38) with a horizontal resolution of 0.1 degree on a regular lon/lat grid. These experiments  
233 employ prescribed velocities and several tracer initial conditions in "offline mode" (i.e. with no  
234 dynamics) to solve the 2D advection diffusion equation without simulating additional processes  
235 (e.g. vertical processes or surface forcing), effectively isolating the effect of lateral eddy stir-

ring. The advecting velocities are linearly interpolated from the Aviso 1/4 deg grid onto the finer model grid and then corrected to be non-divergent following the method described in (9). The effect of this correction is minimal at the mesoscale, but it does introduce small yet significant spurious variability of the basin-scale flow which leads to biases in the diffusivity timeseries. (See Supplementary Materials for details). We therefore use these tracer experiments as an opportunity to validate the SMLT closure, rather than as a direct estimate of realistic temporal variability in the diffusivity.

## 4.5 Osborn-Cox diffusivity

The Osborn-Cox diffusivity (39, 40), denoted  $K_{OC}$ , parameterizes the local down-gradient eddy flux associated with irreversible mixing across tracer fronts. We obtain a dataset of near-surface diffusivities, with a 3 month time resolution, by diagnosing  $K_{OC}$  from the tracer fields of the experiments described above. These tracers are subjected to stirring by the offline velocity field until an equilibrium between the generation and dissipation of tracer variance is reached. Since this equilibrium is established rather rapidly , this technique enables us to resolve changes in mixing on interannual timescales.  $K_{OC}$  is calculated as:

$$K_{OC} = \kappa \frac{\overline{|\nabla q'|^2}}{|\nabla \bar{q}|^2} \quad (5)$$

where  $q$  is a passive tracer (4 realistic and synthetic tracer fields are used; for details see Supplementary Material).  $\kappa$  is the grid-scale diffusivity and the prime represents the mesoscale anomaly. To robustly separate the large scale flow and the mesoscale flow we use a combination of a time average and a spatial filter to define the large scale terms (indicated by an overbar, for more details on the method see Supplementary Material 4.3).

Physically  $K_{OC}$  represents the local enhancement of a small scale diffusivity  $\kappa$  by the creation of lateral tracer gradient variance due to eddy stirring. The small scale diffusivity here

258 is the result of explicit and numerical diffusivity diagnosed as  $63 \text{ m}^2/\text{s}$  from the tracer vari-  
 259 ance budget (9). The ratio  $\overline{|\nabla q'|^2}/|\nabla q|^2$  can be interpreted analogous to the length scales of  
 260 the “effective diffusivity” (41), with large variance in the gradient of the lateral tracer anomaly  
 261 representing a highly filamented tracer field. For the derivation of  $K_{OC}$  and additional discus-  
 262 sion we refer to (9) and references therein. The quantity  $K_{OC}$  is most useful for quantifying  
 263 mixing when the tracer variance budget is characterized predominantly by a local balance be-  
 264 tween variance production and dissipation—which is indeed the case for our experiments (see  
 265 Supplementary Materials for details on the tracer variance budget).

## 266 **4.6 Diffusivity from suppressed mixing length theory**

267 Here we apply SMLT to attempt to reconstruct the temporal variability observed in  $K_{OC}$  from  
 268 simple physical principles. We hypothesize that the main aspects of the flow which vary in  
 269 time are  $U$  and  $u_{rms}$  and assume that  $L_{eddy}$ ,  $\gamma$ ,  $\Gamma$ , and  $c$  do not vary in time. In this case, the  
 270 diffusivity formula (4) can be written as

$$K(u_{rms}, U) = K_0(u_{rms})S(U) \quad (6)$$

271 For small-amplitude variability, we can linearize this to find

$$\Delta K = \underbrace{\overline{K_0}\Delta S}_{\text{Large Scale Contribution}} + \underbrace{\overline{S}\Delta K_0}_{\text{Small Scale Contribution}} \quad (7)$$

272 where the overbar indicates the long-term time mean and the  $\Delta$  a time fluctuation.

273 We find  $\Delta K_0$  and  $\Delta S$  by Taylor expansion.  $\Delta K_0$  is trivial:

$$\Delta K_0 = \frac{\partial K_0}{\partial u_{rms}} \Delta u_{rms} = \Gamma L_{eddy} \Delta u_{rms} \quad (8)$$

274 The suppression factor requires a bit more algebra:

$$\Delta S = \frac{\partial S}{\partial U} \Delta U = 2\alpha(c - \bar{U}) \bar{S}^2 \Delta U . \quad (9)$$

255 If not otherwise noted, the diffusivity variability and its contributions (e.g.  $\Delta K$ ,  $\bar{K}_0 \Delta S$ ,  
266  $\bar{S} \Delta K_0$ ) are shown with the mean diffusivity  $\bar{K}_{mix}$  added.

## 277 4.7 Tracer Experiment Results

278 The time-mean  $K_{OC}$  over the 1993-2016 period (Fig. 4a) agrees well with prior studies (9),  
279 but our dataset also reveals strong interannual variability. The interannual range (the difference  
280 between the 10th and 90th percentiles ) of  $K_{OC}$  resembles the spatial structure of the mean  
281 (Fig. 4b). High variability  $O(1000 \text{ m}^2 \text{ s}^{-1})$  is found in the equatorial regions, the western  
282 boundary current extensions, and parts of the Indian Ocean. The subtropical and subpolar basins  
283 show lower variability,  $O(100 \text{ m}^2 \text{ s}^{-1})$ . Most locations in the global ocean show interannual  
284 variability with a magnitude on the same order of the mean diffusivity, suggesting that temporal  
285 variability is of high importance to characterize global surface diffusivities.

286 For a more detailed analysis we will focus on data averaged in space over two boxes in  
287 the subtropics of the North and South Pacific (see Figure 5 for locations). Here the large scale  
288 velocities vary coherently over the region as a consequence of the divergence correction applied  
289 (see Supplementary Material). This property likely causes the temporal variability in  $K_{OC}$  to  
290 be unrealistic, e.g. this is not how diffusivities behaved over the last 20 years, but it serves  
291 as a testbed to compare different methods of diagnosing diffusivities. In particular we will  
292 focus on the effect of large scale flow suppression on surface diffusivities. While the temporal  
293 evolution of the large scale velocities in the tracer experiment might be unrealistic, the amplitude  
294 ( $\pm 0.05 \text{ m/s}$ , Figure 5a/b) is within changes observed from altimetry from interannual changes  
295 up to long-term trends (Figure 5c). The resulting changes in surface diffusivity are large, up

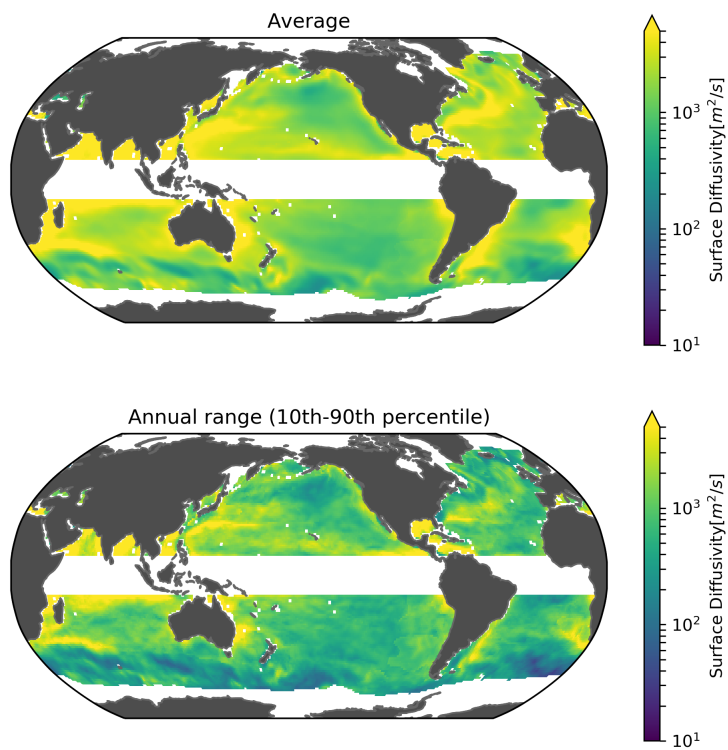


Figure 4:  $K_{OC}$  maps. Same maps as in Figure 1, but for the surface diffusivities derived from the passive tracer experiment. Note that these were derived from the divergence corrected velocities (for details see text). **I need to redo these with boxes. Left is a) and right is b)...**

296 to  $2000\text{m}^2/\text{s}$  in the chosen example boxes. This represents a large change compared to the  
297 approximate baseline diffusivity values of  $1000\text{-}1500\text{m}^2/\text{s}$

298 Notably, strong excursions of  $K_{OC}$  are closely following episodes of increased westward  
299 velocity (Figure 5, shows the velocities inverted to aid visual comparison), consistent with an  
300 increase in the suppression factor from suppressed mixing length theory (SMLT, Eqn 3). The  
301 variations in small scale velocities ( $u_{rms} = \sqrt{2EKE}$ ) seem to have less relation to the diag-  
302 nosed diffusivities, particularly for large diffusivity events. The pronounced seasonal cycle in  
303  $u_{rms}$  (not shown) is not mirrored in the  $K_{OC}$  values, possibly indicating that on time scales  
304 shorter than seasonal, variance advection becomes an important term in the variance budget  
305 and the concept of a diffusivity might break down. In this study however we will focus on  
306 interannual variability and the subject of seasonal variability is left for future study. Analysis  
307 of the full tracer variance budget from the tracer experiment suggest that temporal variations  
308 on interannual and longer time scales can be represented by a diffusivity approach (for details  
309 see Appendix) and thus in the remainder of this study we will focus on interannual and longer  
310 signals, by lowpass filtering all monthly data with a month Gaussian window.

311 The relationship between the large scale velocity and  $K_{OC}$  holds in many regions globally  
312 as indicated by large correlation coefficients shown in Figure( 5c). The negative correlation  
313 between large scale zonal velocities and  $K_{OC}$  is generally strongest in the subtropical Pacific,  
314 but values remain high throughout the world ocean. The correlation between  $u_{rms}$  (Figure( 5d)  
315 does not show values as high as the large scale velocities, but most regions of the oceans show a  
316 moderate and significant correlation, suggesting that temporal variability caused by small scale  
317 velocity fluctuations is not negligible.

318 But is this finding applicable to the real ocean? To answer this question, we will need to use  
319 the SMLT derived  $K_{mix}$ , since that can be applied directly to observed, uncorrected velocity  
320 fields. We will thus compare the results from the tracer based Osborn-Cox diffusivity ( $K_{OC}$ ) to

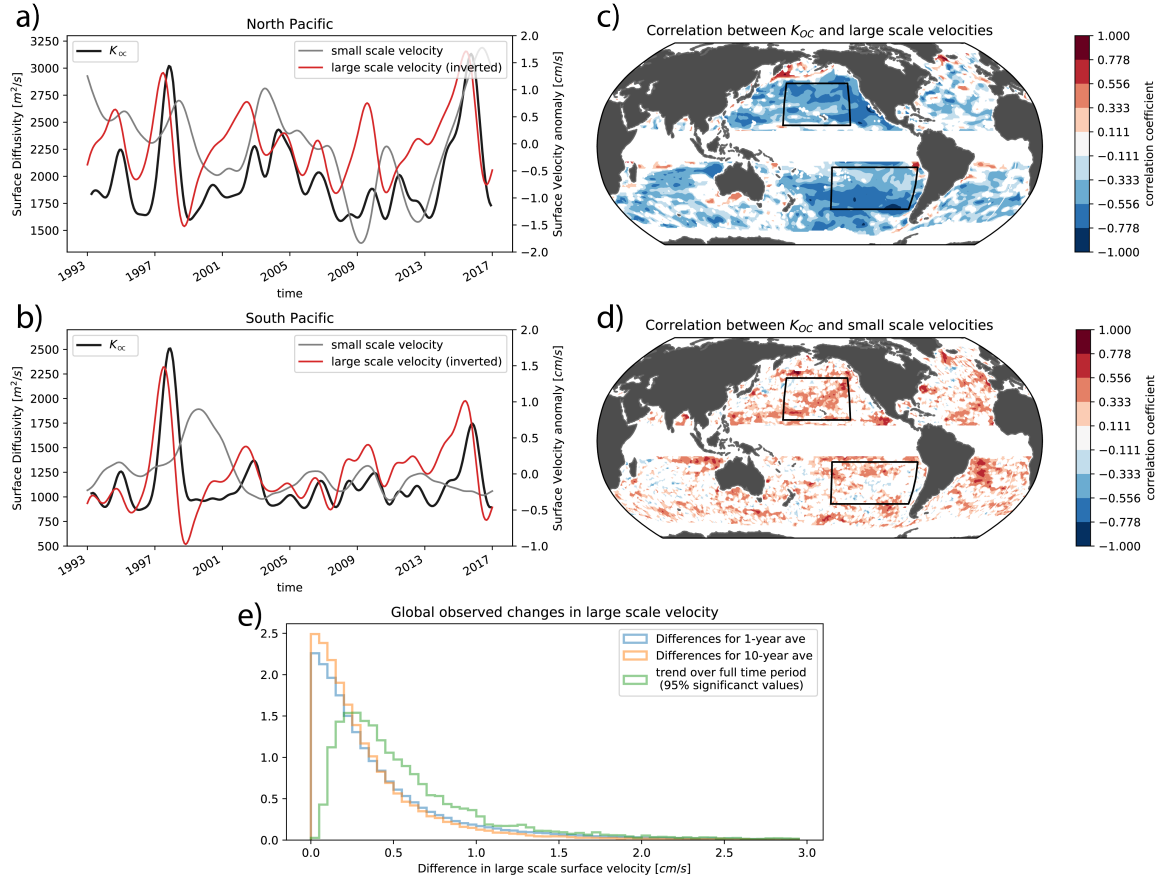


Fig. 5: Relationship of  $K_{OC}$  to small- and large-scale velocities. a-b) Timeseries of Osborn-Cox Diffusivity ( $K_{OC}$ , black), large scale velocities anomalies ( $u$ , red) and small scale velocity anomalies ( $u_{rms}$ , gray) for the North and South Pacific subtropical boxes shown in map panels. c) Correlation coefficient between surface diffusivity ( $K_{OC}$ ) and large scale velocities. d) Correlation coefficient between surface diffusivity ( $K_{OC}$ ) and small scale velocity fluctuations. All quantities are lowpass filtered with a Gaussian window. Note that all values are taken from the tracer experiments, hence large scale velocity fluctuations are influenced by the divergence correction (see text for details). e) shows the global distribution of changes in surface velocities (from observed product) for various time averaging intervals and the long term trend over the full time period of Aviso data. All data shown are smoothed with a 4 month Gaussian window.

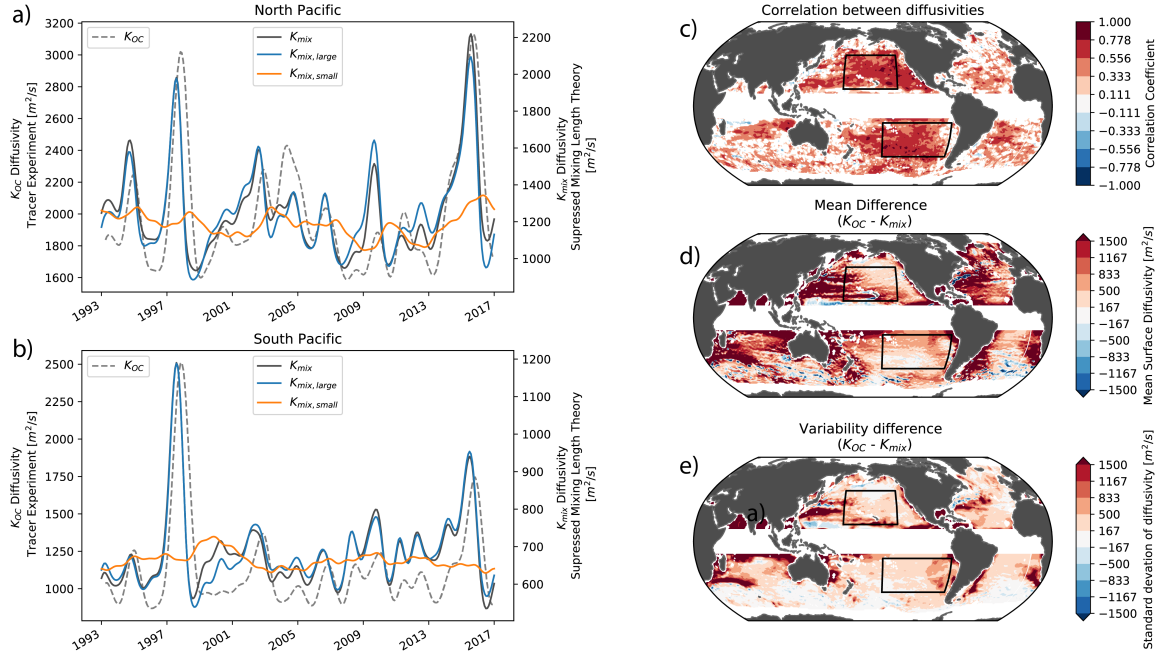


Figure 6: Comparison between  $K_{OC}$  and  $K_{mix}$ . a-b) Timeseries of surface diffusivities, comparing  $K_{OC}$  (blue),  $K_{mix}$  (orange), the variability due to large scale velocity suppression (green) and the variability due to small scale velocity fluctuations averaged over the same boxes as Fig. 5. Note the different axes for the  $K_{OC}$  values (left) and  $K_{mix}$  (right). c) shows the correlation map between  $K_{OC}$  and  $K_{mix}$ . d) shows the offset between the time average of  $K_{OC}$  and  $K_{mix}$ . e) shows the difference between the temporal standard deviation of  $K_{OC}$  and  $K_{mix}$ . All data shown are smoothed with a 4 month Gaussian window.

321  $K_{mix}$  to verify that the main features of variability are well captured.

322 Fig. 6 shows that the relative variability (e.g. the timing of anomalies) in diffusivities is well  
 323 captured, while the mean diffusivity and the amplitude of diffusivity anomalies are considerably  
 324 different between the two estimates of surface diffusivity. Fig. 6a-b shows the strong covariance  
 325 between  $K_{OC}$  and  $K_{mix}$ , in particular the variability  $K_{mix}$  caused by the suppression of the large  
 326 scale flow. Globally the correlation between the two estimates is high in most regions (Fig. 6c),  
 327 while time mean values of  $K_{OC}$  are mostly higher, sometimes over  $1000\text{m}^2/\text{s}$  (Fig. 6 d, compare  
 328 also the different y axes in a-b). In most regions the amplitude of variability is larger for  $K_{OC}$   
 329 although there are exceptions. Overall these results indicate that both methods agree well on

330 the sign of anomalies, but the actual absolute values can differ substantially between estimates,  
331 mostly with higher values and variability in the  $K_{OC}$ .

332 This result is highly encouraging, since it confirms that the SMLT is able to capture time  
333 variations in surface diffusivity, allowing the application of SMLT to the realistic (uncorrected)  
334 velocities.

335 **References**

- 336 1. J. Marshall, K. Speer, *Nature Geoscience* **5**, 171 (2012).
- 337 2. J. Marshall, J. R. Scott, A. Romanou, M. Kelley, A. Leboissetier, *Ocean Modelling* **111**, 1  
338 (2017).
- 339 3. S. Groeskamp, B. M. Sloyan, J. D. Zika, T. J. McDougall, *Journal of Physical Oceanogra-*  
340 *phy* (2017).
- 341 4. M. P. McCann, A. J. Semtner, R. M. Chervin, *Climate Dynamics* **10**, 59 (1994).
- 342 5. D. Stammer, *Journal of Physical Oceanography* **28**, 727 (1998).
- 343 6. A. M. Treguier, J. Deshayes, C. Lique, R. Dussin, J. M. Molines, *Journal of Geophysical*  
344 *Research: Oceans* **117**, n/a (2012).
- 345 7. A. Gnanadesikan, M.-A. Pradal, R. P. Abernathey, *Geophysical Research Letters* **42**, 4249  
346 (2015).
- 347 8. A. Gnanadesikan, A. Russell, M.-A. Pradal, R. Abernathey, *Journal of Advances in Mod-*  
348 *eling Earth Systems* **9**, 2493 (2017).
- 349 9. R. P. Abernathey, J. Marshall, *Journal of Geophysical Research: Oceans* **118**, 901 (2013).
- 350 10. V. Zhurbas, *Journal of Geophysical Research* **109**, C05015 (2004).
- 351 11. I. I. Rypina, I. Kamenkovich, P. S. Berloff, L. J. Pratt, *Journal of Physical Oceanography*  
352 **42**, 2206 (2012).
- 353 12. S. T. Cole, C. Wortham, E. Kunze, W. B. Owens, *Geophysical Research Letters* **42**,  
354 2015GL063827 (2015).

- 355 13. S. Groeskamp, R. P. Abernathey, A. Klocker, *Geophysical Research Letters* **43**,  
356 2016GL070860 (2016).
- 357 14. D. Stammer, C. Wunsch, K. Ueyoshi, *Journal of Physical Oceanography* (2006).
- 358 15. J. Busecke, R. P. Abernathey, A. L. Gordon, *Journal of Physical Oceanography* **47**, 737  
359 (2017).
- 360 16. G. I. Taylor, *Monthly Weather Review* **43**, 315 (1915).
- 361 17. R. Ferrari, M. Nikurashin, *Journal of Physical Oceanography* **40**, 1501 (2010).
- 362 18. A. Klocker, R. Abernathey, *Journal of Physical Oceanography* **44**, 1030 (2013).
- 363 19. R. Abernathey, J. Marshall, M. Mazloff, E. Shuckburgh, *Journal of Physical Oceanography*  
364 **40**, 170 (2010).
- 365 20. R. Seager, Y. Kushnir, N. H. Naik, M. A. Cane, J. Miller, *Journal of Climate* **14**, 4249  
366 (2001).
- 367 21. M. H. England, *et al.*, *Nature Climate Change* **4**, 222 (2014).
- 368 22. J. W. Hurrell, *Science* **269**, 676 (1995).
- 369 23. N. H. Saji, T. Yamagata, *Climate Research* **25**, 151 (2003).
- 370 24. A. L. Gordon, R. D. Susanto, K. Vrana, *Nature* **425**, 824 (2003).
- 371 25. A. L. Gordon, *et al.*, *Geophysical Research Letters* **39** (2012).
- 372 26. A. L. Gordon, *et al.*, *Geophysical Research Letters* **24**, 2573 (1997).
- 373 27. Q. Song, A. L. Gordon, M. Visbeck, *Journal of Physical Oceanography* **34**, 772 (2004).

- 374 28. E. A. Wilson, A. L. Gordon, D. Kim, *Journal of Geophysical Research: Atmospheres* **118**,  
375 2588 (2013).
- 376 29. N. J. Mantua, S. R. Hare, Y. Zhang, J. M. Wallace, R. C. Francis, *Bulletin of the American  
377 Meteorological Society* **78**, 1069 (1997).
- 378 30. M. Visbeck, J. Marshall, T. Haine, M. Spall, *Journal of Physical Oceanography* **27**, 381  
379 (1997).
- 380 31. D. Roemmich, J. Gilson, *Journal of Physical Oceanography* **31**, 675 (2001).
- 381 32. X. Liang, C. Wunsch, P. Heimbach, G. Forget, *Journal of Climate* **28**, 3821 (2015).
- 382 33. L. Bopp, M. Lvy, L. Resplandy, J. B. Salle, *Geophysical Research Letters* **42**, 6416 (2015).
- 383 34. P. Brandt, *et al.*, *Biogeosciences Discussions* **11**, 12069 (2014).
- 384 35. C. O. Dufour, *et al.*, *Journal of Physical Oceanography* **45**, 3057 (2015).
- 385 36. S. Hoyer, C. Fitzgerald, J. Hamman, *et al.*, xarray (2018).
- 386 37. R. Abernathey, *et al.*, xgcm (2017).
- 387 38. J. Marshall, A. Adcroft, C. Hill, L. Perelman, C. Heisey, *Journal of Geophysical Research:  
388 Oceans (19782012)* **102**, 5753 (1997).
- 389 39. T. R. Osborn, C. S. Cox, *Geophysical Fluid Dynamics* **3**, 321 (1972).
- 390 40. N. Nakamura, *Journal of the Atmospheric Sciences* **58**, 3685 (2001).
- 391 41. N. Nakamura, *Journal of the Atmospheric Sciences* **53**, 1524 (1996).
- 392 42. M. Germano, *Journal of Fluid Mechanics* **238**, 325 (1992).

393 43. G. L. Eyink, H. Aluie, *Physics of Fluids* **21**, 115107 (2009).

394 44. H. Aluie, *arXiv preprint arXiv:1808.03323* (2018).

395 45. S. Schmidtko, G. C. Johnson, J. M. Lyman, *Journal of Geophysical Research: Oceans* pp.  
396 1–15 (2013).

## 397 Acknowledgments

398 J.B. acknowledges support from NASA award NNX14AP29H. R.P.A. acknowledges support  
399 from NSF OCE 1553593. We thank Sjoerd Groeskamp for valuable comments on this draft.  
400 All authors contributed to the interpretation of the results and writing of the manuscript. The  
401 authors declare that they have no competing financial interests. The code to reproduce these  
402 results using the MITgcm will be provided in a github repository (<https://github.com/>  
403 [jbusecke/mitgcm\\_surface\\_tracer](https://github.com/jbusecke/mitgcm_surface_tracer)). The dataset presented is available under <http://dx.doi.org/10.6084/m9.figshare.4928693>.

## 405 Supplementary materials

406 Figs. S7 to S9

407 References (42-44)

408 **5 Supplementary Material**

409 **5.1 Discussion of velocity biases**

410 The divergence correction does not affect the eddy properties - the small and short scale fluctu-  
411 ations as indicated by the almost identical eddy kinetic energy (EKE, not shown) between the  
412 corrected product and the uncorrected, also described in earlier work using this method (9). It  
413 does however introduce basinwide large scale biases, which are particularly pronounced during  
414 positive and negative phases of ENSO in the Pacific (Fig. 7). The amplitude of these biases is  
415 quite small ( $< 2\text{cm/s}$ ). But argued in the main text these small differences will change sur-  
416 face diffusivities considerably. This is particularly important since changes of the large scale  
417 circulation on the magnitude up to  $1\text{cm/s}$  are certainly seen over a wide range of regions and  
418 timescales in the global ocean (e.g. Fig. 5). Due to the large scale velocity bias, results from  
419 the tracer experiment might not reproduce realistic changes in diffusivity, particularly in the  
420 subtropical basins. While the large scale structure of interannual variations is not realistic, the  
421 amplitude is within the observed variability in surface currents (internannual and longer), as  
422 seen in Fig. 7. It however, serves well as a sensitivity testbed in which the validity of the SMLT-  
423 derived diffusivities can be compared to an independent estimate of surface diffusivities, to gain  
424 confidence about applying SMLT to observed velocities.

425 **5.2 Osborn-Cox Diffusivity based on Smoothing Operator**

426 Nakamura (2001) (40) defines a scalar eddy diffusivity based on the tracer variance budget  
427 under generic Reynolds averaging. Our experiments use a convolution filter to apply spatial  
428 smoothing. Convolution is not a Reynolds average, so here we re-derive Nakamura's result for  
429 our filter-based approach, following the approach outlined in (42, 43).

430 Our smoothing operator, indicated by angle brackets, is defined by spatial convolution. For

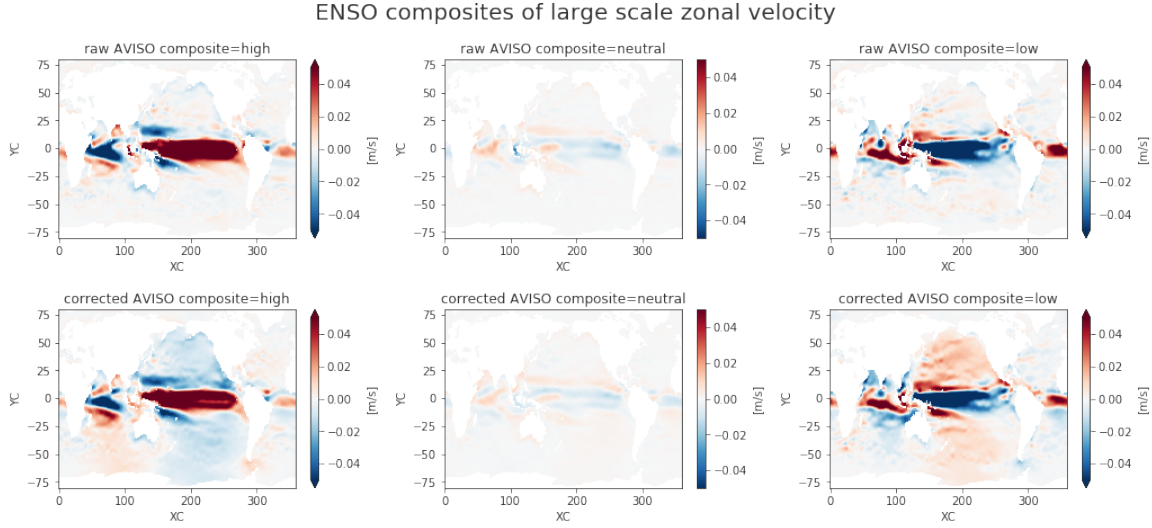


Fig. 7: Velocity bias introduced by divergence correction. The columns represent composite averages of high(left), neutral(center) and low(right) NINO3.4 indicies for the uncorrected - e.g. observed - velocities (upper) and the divergence corrected velocities (lower) used for the tracer experiment.

431 a scalar field  $f(\mathbf{x}, t)$ , the smoothed field is

$$\langle f \rangle = \int f(\mathbf{x}', t) \mathcal{G}(\mathbf{x} - \mathbf{x}'; \ell) d\mathbf{x}. \quad (10)$$

432 We use a Gaussian Kernel in 2D, defined as

$$\mathcal{G}(\mathbf{x}; \sigma) = \frac{1}{2\pi\sigma^2} e^{-|\mathbf{x}|^2/2\sigma^2} \quad (11)$$

where  $\sigma$  is the standard deviation. Smoothing is not a Reynolds operator, because

$$\langle \langle f \rangle \rangle \neq \langle f \rangle \quad (12)$$

$$\langle f \langle g \rangle \rangle \neq \langle f \rangle \langle g \rangle. \quad (13)$$

For second order statistics, we define the small-scale component via the operator  $\tau$ , defined as

$$\tau(f, g) = \langle fg \rangle - \langle f \rangle \langle g \rangle \quad (14)$$

$$(15)$$

<sup>433</sup> The quantity  $\tau(f, f)$  can be thought of as the small-scale variance, while  $\langle f \rangle^2$  is the large-scale  
<sup>434</sup> variance. They sum to give the total variance. The third-order fluctuation quantities are given  
<sup>435</sup> by:

$$\tau(f, g, h) = \langle f g h \rangle - \langle f \rangle \tau(g, h) - \langle g \rangle \tau(f, h) - \langle h \rangle \tau(f, g) - \langle f \rangle \langle g \rangle \langle h \rangle . \quad (16)$$

<sup>436</sup> Note that, since Reynolds averaging (e.g. time average) commutes with convolution, we can  
<sup>437</sup> and do add time averaging to our smoothing operation with no change to the derivations below.

<sup>438</sup> In many papers, the smoothing operation is applied to the momentum equation to derive  
<sup>439</sup> a large-scale and small scale kinetic energy equation (42, 43) Here we apply it to the passive  
<sup>440</sup> tracer equation:

$$\partial_t \theta + \mathbf{u} \cdot \nabla \theta = \nabla \cdot \kappa \nabla \theta + s \quad (17)$$

<sup>441</sup> where  $\kappa$  is the molecular diffusivity  $s$  is any (non-diffusive) source or sink. The flow is incom-  
<sup>442</sup> pressible:  $\nabla \cdot \mathbf{u} = 0$ . Also,  $\nabla \cdot \langle \mathbf{u} \rangle = 0$  The smoothed version is

$$\partial_t \langle \theta \rangle + \langle \mathbf{u} \rangle \cdot \nabla \langle \theta \rangle = -\nabla \cdot \tau(\mathbf{u}, \theta) + \nabla \cdot \kappa \nabla \langle \theta \rangle + \langle s \rangle . \quad (18)$$

<sup>443</sup> The quantity  $\tau(\mathbf{u}, \theta)$  plays the role of the Reynolds flux. The total variance is  $\langle \theta^2 \rangle / 2$ . Using the  
<sup>444</sup>  $\tau$  operator, we can express it as the sum of a small-scale component and large-scale component.  
<sup>445</sup> The small-scale tracer variance is given by

$$\frac{1}{2} \tau(\theta, \theta) = \frac{1}{2} (\langle \theta^2 \rangle - \langle \theta \rangle^2) . \quad (19)$$

<sup>446</sup> To derive the tracer-variance equation, we start by multiplying (17) by  $\theta$  and then smoothing.  
<sup>447</sup> We get

$$\partial_t \frac{\langle \theta^2 \rangle}{2} + \nabla \cdot \langle \mathbf{u} \frac{\theta}{2} \rangle = \nabla \cdot \kappa \frac{\langle \theta^2 \rangle}{2} - \kappa \langle |\nabla \theta|^2 \rangle . \quad (20)$$

<sup>448</sup> Next we multiply (18) by  $\langle \theta \rangle$  to find

$$\partial_t \frac{\langle \theta \rangle^2}{2} + \langle \mathbf{u} \rangle \nabla \cdot \frac{\langle \theta \rangle^2}{2} = -\theta \nabla \cdot \tau(\mathbf{u}, \theta) + \nabla \cdot \kappa \nabla \frac{\langle \theta \rangle^2}{2} - \kappa \langle |\nabla \theta|^2 \rangle . \quad (21)$$

In order to get to an equation for  $\tau(\theta, \theta)/2$ , we need to subtract (21) from (20). There is a bit of algebra to work out. First we note that

$$\langle \theta \rangle \nabla \tau(\mathbf{u}, \theta) = \nabla \cdot \langle \theta \rangle \tau(\mathbf{u}, \theta) - \tau(\mathbf{u}, \theta) \cdot \nabla \langle \theta \rangle . \quad (22)$$

Now we put all terms with a  $\mathbf{u}$  in them on the left-hand side of the equation and simplify, using the third-order fluctuation definition. We obtain

$$\nabla \cdot \left[ \langle \mathbf{u} \frac{\theta}{2} \rangle - \langle \theta \rangle \tau(\mathbf{u}, \theta) - \langle \mathbf{u} \rangle \frac{\langle \theta \rangle^2}{2} \right] + \tau(\mathbf{u}, \theta) \cdot \nabla \langle \theta \rangle \quad (23)$$

$$= \nabla \cdot \left[ \langle \mathbf{u} \rangle \frac{\tau(\theta, \theta)}{2} + \frac{1}{2} \tau(\mathbf{u}, \theta, \theta) \right] + \tau(\mathbf{u}, \theta) \cdot \nabla \langle \theta \rangle . \quad (24)$$

The terms proportional to  $\kappa$  give

$$\nabla \cdot \kappa \nabla \left( \frac{\langle \theta^2 \rangle}{2} - \frac{\langle \theta \rangle^2}{2} \right) - \kappa \langle |\nabla \theta|^2 \rangle + \kappa |\nabla \langle \theta \rangle|^2 \quad (25)$$

$$= \nabla \cdot \kappa \nabla \frac{\tau(\theta, \theta)}{2} - \kappa \tau[(\nabla \theta)^T, \nabla \theta] \quad (26)$$

Putting it all together, we find

$$\partial_t \frac{\tau(\theta, \theta)}{2} + \nabla \cdot \left[ \langle \mathbf{u} \rangle \frac{\tau(\theta, \theta)}{2} + \frac{1}{2} \tau(\mathbf{u}, \theta, \theta) - \kappa \nabla \frac{\tau(\theta, \theta)}{2} \right] + \tau(\mathbf{u}, \theta) \cdot \nabla \langle \theta \rangle = -\kappa \tau((\nabla \theta)^T, \nabla \theta) \quad (27)$$

449 If we average over the whole domain and assume that the statistics are stationary in time,  
450 we are left with the balance

$$\int \tau(\mathbf{u}, \theta) \cdot \nabla \langle \theta \rangle d\mathbf{x} = - \int \kappa \tau((\nabla \theta)^T, \nabla \theta) d\mathbf{x} . \quad (28)$$

451 Because the right-hand side is negative definite,  $\tau(\mathbf{u}, \theta)$  must, on average, have the opposite  
452 sign to  $\nabla \langle \theta \rangle$ . That suggests that  $\tau(\mathbf{u}, \theta)$  can be represented via down-gradient diffusion.

453 Following (40), we can try to separate the part of this flux associated with reversible pro-  
454 cesses from the down-gradient flux due to irreversible mixing. We let

$$\tau(\mathbf{u}, \theta) = -(K_k + K_e) \nabla \langle \theta \rangle . \quad (29)$$

455 Which are defined via

$$K_k = \frac{\partial_t \tau(\theta, \theta) + \nabla \cdot [\langle \mathbf{u} \rangle \tau(\theta, \theta) + \tau(\mathbf{u}, \theta, \theta) - \kappa \nabla \tau(\theta, \theta)]}{2|\nabla \langle \theta \rangle|^2} \quad (30)$$

456 and

$$K_e = \kappa \frac{\tau((\nabla \theta)^T, \nabla \theta)}{|\nabla \langle \theta \rangle|^2} \quad (31)$$

457 or

$$K_m = \kappa \frac{\langle |\nabla \theta|^2 \rangle}{|\nabla \langle \theta \rangle|^2} = K_e + \kappa. \quad (32)$$

458 The quantity  $K_m$  is equivalent to the Osborn-Cox diffusivity of (9).

459 The main shortcoming of this approach is that our convolution operator does not commute  
460 precisely with differential operators on the sphere (44). This introduces small but nonzero  
461 residuals in the tracer variance equation.

### 462 5.3 Osborn-Cox cross frontal diffusivity using multiple tracers

463 The spatial distribution of the scalar lateral surface diffusivities ( $K_{OC}$ ) depends on the initial  
464 tracer field  $q_0$ , reflecting the anisotropy of the full diffusivity tensor projected onto the back-  
465 ground gradient (9). We compute the diffusivities for 4 experiments with different initial tracer  
466 fields  $q_0$ :

467 •  $K_{OC,LAT} q_0$  is a linear function of the latitude

468 •  $K_{OC,PSI} q_0$  is the mean horizontal streamfunction, based on the the mean dynamic topog-  
469 raphy from Aviso altimetry (9)

470 •  $K_{OC,SST} q_0$  is the mean climatological sea surface temperature (SST) (45)

471 •  $K_{OC,SSS} q_0$  is the mean climatological sea surface salinity (SSS) (45)

472 Each field is linearly interpolated onto the model grid.

473 A previous study using this methodology has focused on the spatial variability of the long-  
474 term mean (9). Using a different diagnostic but identical model setup (15) documented time  
475 variability in eddy diffusivities in the subtropical. In order to resolve spatio-temporal variabil-  
476 ity, in this manuscript we combine some of the methods from both studies above: For each  
477 experiment (defined by the initial tracer field  $q_0$ ), we compute two passive tracers ( $q$ ) which are  
478 initialized identically and reset with equal and regular time intervals (390 days) but the reset  
479 phase of one tracer is shifted by half a reset interval, similar to (15). After each of the respective  
480 reset points the initial spin up phase (30 days) is removed due to the dominating role of the ten-  
481 dency term in the tracer variance budget (for details see (9, 15)). This results in a 5-dimensional  
482 array of diffusivities

$$K_{OC}\{\text{longitude}(lon), \text{latitude}(lat), \text{time}(ti), \text{tracer}(q), \text{initial condition}(q_0)\} \quad (33)$$

483 Results from experiments with several initial conditions mostly differ in terms of overall  
484 magnitude and spatial structure (Fig. 8a), while temporal variability is very coherent across  
485 experiments on interannual and longer time scales, particularly in the subtropics of the Pacific  
486 (Fig. 8b).

487 This means that the temporal changes in diffusivity are driven by the velocity field. We  
488 compute a minimum diffusivity  $K_{min}$  across all four tracer experiments by selecting the lowest  
489 time-averaged diffusivity at each grid point.  $K_{min}$  is interpreted as the cross-frontal diffusivity  
490 (closely related to the minor axis of the diffusivity tensor), which is most relevant to identify  
491 mixing barriers (9). For simplicity, the rest of the manuscript will refer to  $K_{min}$  as  $K_{OC}$ ; no  
492 results of single tracer experiments are used outside of the methods section. Details on the  
493 uncertainty of  $K_{min}$  are given below.

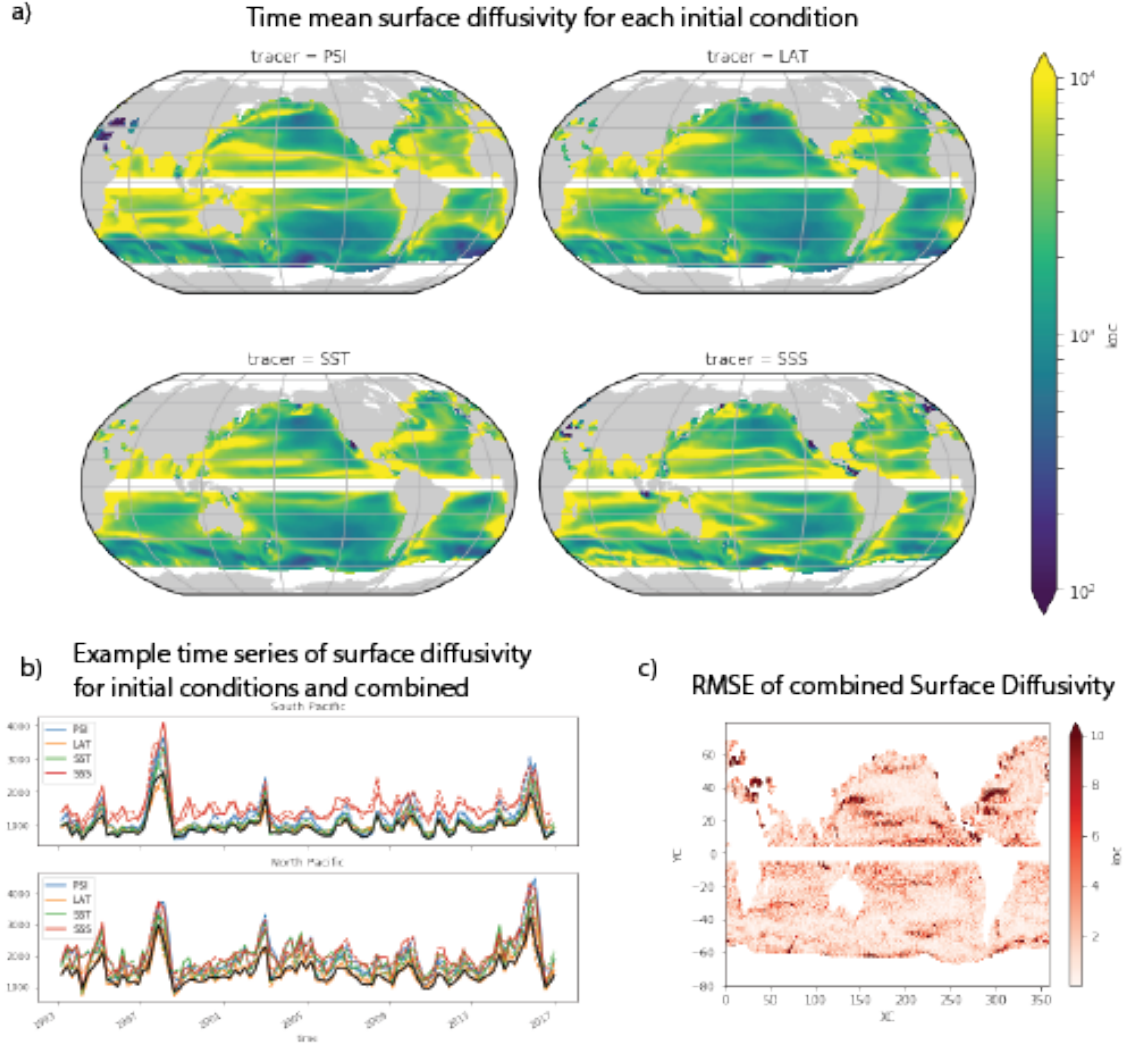


Fig. 8: Comparison of  $K_{OC}$  results for different initial conditions. a) Time mean surface diffusivity for each initial condition ('tracer') used in  $[m^2/s]$ . b) Example time series in the North and South Pacific boxes used in the main text (see Figure 5). c) The root mean square deviations corresponding to the two tracers used as well as the various initial conditions. For details see text.

494 The root mean square error between tracers for each initial condition, defined as

$$RMSE_{tr,q_0} = \sqrt{\langle (K_{OC}\{q, q_0\} - \langle K_{OC}\{q_0\} \rangle_q)^2 \rangle_{ti,q_0}} \quad (34)$$

495 is minor compared to the mean diffusivities. The  $RMSE_{q,q_0}$  (not shown) is mostly smaller than  
496 2% of the local mean of  $K_{OC}$ . We quantify the uncertainty of  $K_{min}$  similar to Eq. 34 as

$$RMSE = \sqrt{\langle (\langle K_{OC} \rangle_q - \langle K_{OC} \rangle_{q,q_0})^2 \rangle_{ti}} \quad (35)$$

497 The estimated uncertainty is smaller than 10% almost everywhere (Fig. 8c). Most importantly  
498 the results presented in this dataset show very similar temporal evolution, indicating that the  
499 variability is indeed caused by the velocity field variability, and not the choice of initial condi-  
500 tion.

## 501 **6 Tracer Variance Budget**

502 In order to use a diffusivity to parameterize the transport by mesoscale eddies, the main balance  
503 in the tracer variance budget (derived and explained in detail in Abernathey and Marshall 2013  
504 (9)), needs to be between variance production and dissipation. To confirm that this balance holds  
505 we computed the full tracer variance budget for all initial conditions of the tracer experiment  
506 (described above) for 3 month averages like in the main text, and in fact we see that for all tracers  
507 the balance holds both spatially (see maps in Figure 9 upper three rows) but also temporally as  
508 shown in the timeseries of dissipation and production, shown in the lower two rows of Figure 9,  
509 for values averaged in the previously used boxes in the North and South Pacific (see Figure 5),  
510 where strong variability in the surface diffusivity is seen.

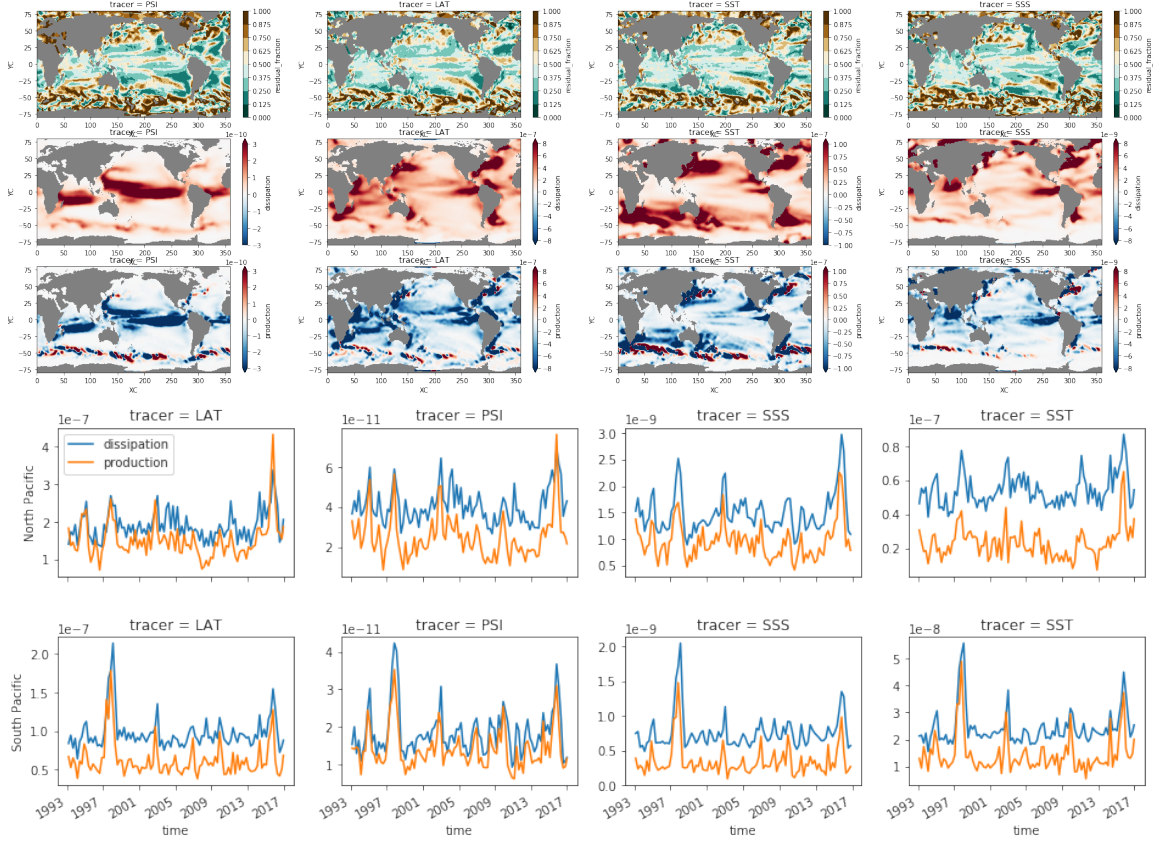


Fig. 9: Validation of Tracer Variance budget. Columns represent the 4 initial conditions used for the tracer experiment (see above for details). The first row shows the residual fraction defined as  $\frac{|production+dissipation|}{|production|+|dissipation|}$ . The second and third row show the dissipation and production term respectively as a long term average. The lower two rows show timeseries of both terms in the previously used example boxes (see e.g. Figure 5), with the dissipation inverted. These show that for the large excursions in the Osborn-Cox diffusivity (described in main text), both terms increase(decrease), thus maintaining the balance and justifying the diffusive approach.